Bull. Chem. Soc. Ethiop. **2025**, 39(3), 515-534.
DOI: https://dx.doi.org/10.4314/bcse.v39i3.10

ISSN 1011-3924
Printed in Ethiopia
Online ISSN 1726-801X

IMPACT OF GRAPHENE OXIDE INTEGRATION WITH ZNO NANOPARTICLES ON ITS PHOTOCATALYTIC, ANTIMICROBIAL, AND ANTIOXIDANT ACTIVITIES

Adugna Olani[1], Jabessa Nagasa Guyasa[1], Dugasa Jabesa Nemera[1], Mulugeta Tesema Efa[2] and Tamene Tadesse Beyene[1*]

[1]Department of Chemistry, College of Natural Sciences, Jimma University, P.O. Box 378, Jimma-Ethiopia
[2]Department of Chemistry, College of Natural & Computational Science, Dambi Dollo University, P.O. Box 260, Dambi Dollo-Ethiopia

(Received September 11, 2024; Revised November 20, 2024; Accepted November 20, 2024)

ABSTRACT. Zinc oxide nanoparticles (ZnO-NPs) are a type of nanomaterial that is biodegradable and has low toxicity and high compatibility with biological systems. They appear to have great potential for biomedical and photocatalysis applications, especially when compared to other metal oxide nanomaterials. Moreover, ZnO-NPs exhibit strong ultraviolet (UV) absorption properties, are cost-effective, and are easy to synthesize. However, pure ZnO-NPs have several limitations, including a wide energy bandgap, high excitation binding energy, poor photocatalytic activity in the visible range, and significant electron-hole recombination, which restrict their applications. To address these limitations, this study successfully incorporated graphene oxide (GO) into ZnO-NPs. Adding 4% GO reduced the energy band gap from 2.87 eV to 2.20 eV, significantly enhancing their activities. As a result of the integration, their photocatalytic activity enhanced, degrading 98% of methylene blue dye after 80 minutes of visible light exposure. Furthermore, GO incorporation boosted their antioxidant activity, increasing their half-maximal inhibitory concentrations (IC_{50}) from 38.38% to 51.60%. The nanocomposite exhibited superior antimicrobial activity compared to the pure ZnO-NPs and GO, indicating enhanced antimicrobial effects through GO integration. These enhancements are attributed to the improved band gap, stability, surface functionality, and nanocomposite morphology, as confirmed by various characterization methods.

KEY WORDS: Antimicrobial, Antioxidant, Dye degradation, GO/ZnO nanocomposite, Reactive oxygen species

INTRODUCTION

Water contamination is a significant global issue due to various industries' release of dyes and effluents [1, 2]. Various industries, such as mining, manufacturing, printing, food preparation, and pharmaceuticals, release natural dyes and their wastewater [3, 4]. Besides to this, infectious diseases caused by bacteria and viruses resistant to antibiotics are a significant global health concern [5]. The emergence and spread of antimicrobial resistance (AMR) primarily result from the misuse and overuse of antibiotics [6].

Nanotechnology makes it possible to produce materials smaller than 100 nm, which can be used to address environmental issues and combat multi-drug resistance caused by harmful pathogens [7, 8]. Metal oxide nanoparticles (MONPs) have a wide range of applications, including catalysis, optoelectronics, sensors, antimicrobial agents, and environmental remediation. Some of the most commonly used semiconductor MONPs are Ag_2O, CuO, ZnO, TiO_2, Al_2O_3, CrO_2, and NiO [9-12]. Zinc oxide nanoparticles (ZnO-NPs) have attracted the attention of researchers due to their therapeutic and diagnostic properties [13, 14]. These nanoparticles have several advantages including low toxicity, biodegradability, and cost-effectiveness [15-17]. They can be securely used for numerous purposes like, preservatives in packaging, medicine, photocatalysts, and antimicrobial agents [13, 18]. ZnO-NPs are able to easily penetrate food, kill detrimental microbes, and protect humans from illness. Moreover, they are highly efficient at breaking down

*Corresponding authors. E-mail: tamene.tadesse@ju.edu.et

persistent dyes that cause significant environmental contamination [19]. Conversely, its extensive bandgap of ZnO (approximately 3.36 eV) [10, 20], an excessive exaction binding energy of 60 meV [21, 22], and aggregations limit their potential applications [23]. For example, the photocatalytic efficiency and antimicrobial activities of ZnO have been often very poor because of the fast recombination of the photogenerated electron-hole pairs and the limited photo responding range. Compositing ZnO-NPs with other materials, such as metals, metal oxides, sulfides, polymers, and nanocarbon-based materials, improves their photocatalytic and antimicrobial activities. Several researchers have conducted thorough investigations to address the limitations associated with pure ZnO-NPs and leverage their benefits. Aga and his co-workers doped ZnO-NPs with limited amount of sulfur at various temperatures to reduce its energy bandgaps and enhance its antibacterial activities [10, 24]. Tegenaw *et al.* incorporated carbon dot materials into ZnO-NPs to modify surface charge and enhance their photocatalytic and antimicrobial activities. Consequently, the energy bandgap of the pristine ZnO-NPs was significantly reduced, and its photocatalytic activity was greatly enhanced [9]. Furthermore, research has been instrumental in enhancing the physicochemical characteristics of ZnO-NPs through adjustments in synthetic pathways. Most notably, Supin and colleagues have successfully produced ZnO-NPs utilizing a leaf extract from *Lepidagathis ananthapuramensis*, resulting in enhanced surface properties, stability, and catalytic performance of the product [25]. Other researchers have also modified the morphologies of ZnO to enhance photocatalytic efficiency. Mourya *et al.* used a straightforward one-pot method to prepare ZnO nanoparticles with adjustable morphologies by changing templates, base, and zinc precursor under microwave irradiation which helped them improve the photocatalytic activity [26].

Graphene is a two-dimensional material [27, 28], with exceptional physical and chemical properties such as high specific surface area and optical transparency [29], and thermal conductivity, making it an ideal candidate for hybridization with ZnO [30]. Enhancing ZnO sunlight absorption is crucial through modification with graphene oxide (GO), improving optical, antimicrobial, and antioxidant properties. Morphology alteration of ZnO-NPs using diverse synthesis methods and materials, incorporation enhances their physical and chemical properties [31, 32]. By preparing ZnO nanocomposites, the drawbacks linked to bare ZnO nanoparticles can be abolished [9, 10, 33, 34]. Nanocomposite materials can display unique mechanical, chemical, electrical, optical, and catalytic properties, making them preferable over their respective individual nanoparticles [35, 36].

In this study, we investigated how incorporating GO into ZnO-NPs form nanocomposite materials (graphene oxide (ZnO/GO-NCs)) and affects their energy bandgap and their ability to break down MB through photocatalysis and inhibit microbial growth. We used the sol-gel method to chemically synthesize ZnO-NPs and tested their composites (ZnO/GO). A UV-Vis spectrophotometer was used to assess the optical properties of the produced NPs and their composites, which showed that adding GO increased the maximum absorbance wavelength. As wavelength increased, the energy band gap of ZnO-NPs decreased from 2.87 eV to 2.20 eV. As a result, ZnO/GO-NCs demonstrated improved photocatalytic activity and antimicrobial compared to pure ZnO-NPs. Therefore, it is crucial to develop a simple and effective method to enhance the photocatalytic and antimicrobial efficiency of ZnO while preventing agglomeration. Notably ZnO/GO-NCs demonstrate enhanced photocatalytic, antimicrobial, and antioxidant performance, decreased band gap, and increased efficiencies compared to pristine ZnO-NPs in this study.

EXPERIMENTAL

The physicochemical characterization of ZnO-NPs provides valuable insights into their antimicrobial and toxicological effects. ZnO-NPs were produced using the chemical method (sol-gel) to investigate the impact of GO incorporation. The Sol-gel method is favored for its narrow particle size distribution, uniform nanostructure at low temperatures, and ease of processing,

ensuring high product purity. This technique is widely employed for synthesizing metal nanooxides. By combining ZnO-NPs with chemically synthesized GO and calcining them, ZnO/GO-NCs were produced.

Chemicals

Standard reagent grade chemicals were entirely utilized in this study. For the synthesis and characterizations of ZnO/GO-NCs, the following analytical grade chemicals were used: zinc nitrate hexahydrate ($Zn(NO_3)_2.6H_2O$, ≥ 98%, Loba Chemie Pvt. Ltd), sodium hydroxide (NaOH) ≥ 98%, Blulux Laboratories Ltd., 121005), ethanol (C_2H_5OH, ≥ 99.9%, Loba Chemie), 99.9%, Favor Trading Co. PLC), graphite fine powder (≥ 98%, Xinhai Chemicals), $KMnO_4$ (≥ 99%), H_2SO_4 (99.99%, Fenchem), hydrochloric acid (HCl ≥ 37%, Sigma Aldrich), hydrogen peroxide (H2O2 ≥ 30% w/v, Loba Chemie Pvt. Ltd), phosphoric acid (H_3PO_4, ≥ 85.0%, Xilong Scientific Co., Ltd), Whatman filter 1& (size 10-500 mm), distilled water, and DMSO (≥ 99.99%, Xilong Scientific Co., Ltd).

Instruments

Varieties of laboratory equipment and advanced analytical tools were utilized in this study. To mention some: pH meters, Directed Ray Radiometer (DRAWELL RADIometer-700), XRD with Directed Ray Cu Radiometer (Cu Kα Radiometer (λ = 1.54178 Å), UV-Vis, and FTIR (Ray Spectrometer-200 PLUS-223E12, Detailed Ray Spectrometer) were also used.

Preparations of zinc oxide nanoparticles

ZnO-NPs were prepared via the sol-gel method using zinc nitrate hexahydrate $Zn(NO_3)_2.6H_2O$ as a precursor. Initially, 3 g of $Zn(NO_3)_2.6H_2O$ was dissolved in 25 mL of double-distilled water. Subsequently, 1.5 g of NaOH was dissolved in 70 mL of distilled water and continuously stirred for 1 h. The pH of $Zn(NO_3)_2.6H_2O$ solution was adjusted to 11 by adding the NaOH solution. The solution obtained was centrifuged, and the resulting precipitate was dried at 95 ℃ for 3 h. Subsequently, the white powder was calcined at 300 ℃ in a muffle furnace for three hours, leading to the synthesis of ZnO-NPs.

Preparation of GO

Graphene oxide was prepared using a previously reported method with some modifications [37, 38]. In a typical procedure, graphene oxide (GO) was synthesized using the modified Hummers method from pure graphite powder. Initially, a mixture of 25 mL of H_2SO_4 and 5 mL of phosphoric acid (H_3PO_4) was stirred for 1 h in an ice bath. In addition, 1.5 g of graphite powder were added under constant stirring to the solution. Due to the high intercalation potential of $KMnO_4$ in sulfuric acid, 15 g was added to the solution to initiate the oxidation of graphene layers. During this process, graphite foam was heated to 35 ℃, which led to the observation of gas evolution. The mixture was stirred continuously for 6 hours until it turned dark green. Afterward, it was removed from the ice bath and stirred for an additional hour at 35 ℃ before raising the temperature to 90 ℃. To remove excess $KMnO_4$, 5 mL of hydrogen peroxide (H_2O_2) was slowly added and stirred for 10 min, resulting in an exothermic reaction that caused the solution to cool down. After that, 30 mL of HCl and 10 mL of deionized water (DIW) were added. The mixture was centrifuged at 6000 rpm for 7 min. The liquid layer on top was poured out, and the remaining residue was washed several times with HCl and DIW. The resulting GO solution was then dried in an oven at 50 ℃ for 1 hour to obtain the powdered form of GO.

Preparation of ZnO/GO composites

The ZnO, GO-NPs, and ethanol were utilized as initial materials for synthesizing ZnO/GO-NCs [39]. The combination of GO) effectively prevented ZnO-NPs from clumping together, ensuring strong stability in the surrounding environment. To create ZnO/GO NCs, 0.05 mg of GO powder was dispersed in 10 mL of ethanol, and 0.8 mg ZnO was dispersed in 10 mL of ethanol. The solutions were mixed using an ultrasonic bath for 2 h at room temperature, followed by 3 h of stirring. The final products were centrifuged, washed with ethanol and distilled water, and then dried for 1.5 h. The ZnO/GO-NCs were acquired and then calcined in a furnace at 350 °C for 2 h. The process of creating ZnO/GO-NCs using different solvents as precursors is illustrated in Figure 1. Finally, the ZnO/GO-NCs were characterized by UV-Vis absorption.

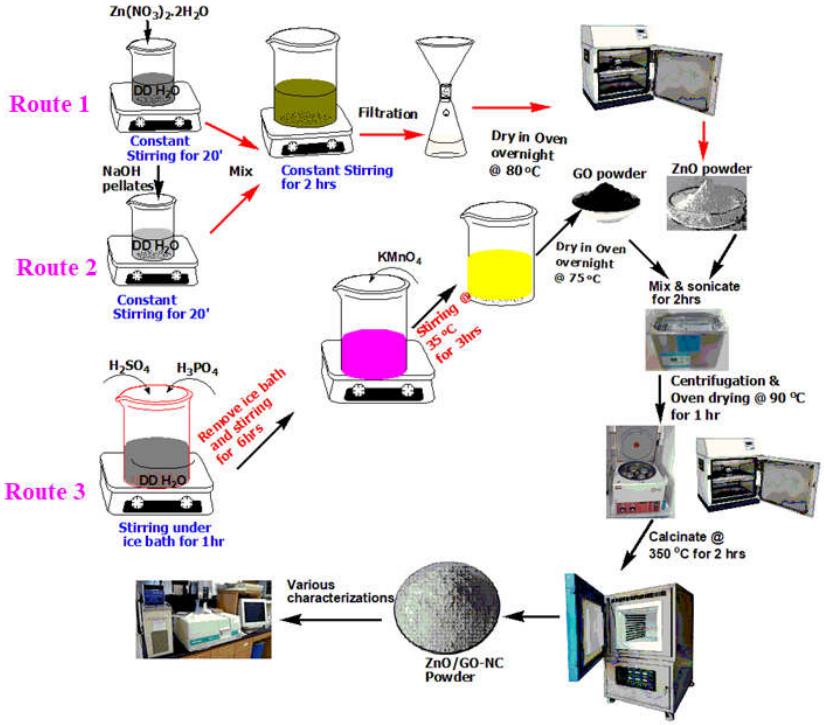

Figure 1. The Schematic illustration of production of pure ZnO-NPs, GO-NPs and ZnO/GO-NCs.

Characterization

Analysis of the pristine ZnO-NPs and ZnO/GO nanocomposites samples was carried out using UV-Vis spectrophotometers, X-ray diffraction (XRD), scanning electron microscopy (SEM), and Fourier-transform infrared spectroscopy (FTIR). For UV-Vis measurements, 0.1 M solution in DDW was used, while solid powders were utilized for XRD and FT-IR. According to Bragg's law, X-ray diffraction requires monochromatic rays. Copper K-alpha, known for its intensity compared to K-beta, was used for enhanced resolution since the technique aims to identify and study material structures. The XRD analysis was performed at 40 kV voltage, 30 mA filament current, and CuKα1 radiation (λ = 1.5418 Å) within the 2θ range of 10º to 70º to decide the crystal

structure and phase arrangement of the manufactured samples. A UV-Vis spectrophotometer was engaged to compute the bandgap energies and measure optical properties. The chemical arrangements of the samples were analyzed using FT-IR in the wave number range of 400-4000 cm^{-1}, while SEM was used to examine the morphologies and microstructures of the samples.

Photocatalytic activities

An investigation of the efficacy of ZnO-NPs and ZnO/GO-NCs in breaking down MB dye was conducted. To conduct the experiment, an MB solution was exposed to direct sunlight between 11:00 and 14:30 in September in Jimma, where the average daily temperature was around 29-32 ^{o}C. Before radiation exposure, the solution and photocatalyst were mixed in darkness for 30 min to establish adsorption-desorption equilibrium. UV-Vis measurements were taken at a specific wavelength to assess the efficiency of removing MB dye. Different concentrations of the photocatalyst were added to a stock solution with 10 mg/L of MB dye in double distilled water. The point of zero charges (pzc) is the pH value for a neutral absorbent surface with zero charges. The process of determining pzc involves monitoring the particles' electrophoretic mobility and the suspension's pH while conducting acid-base titrations on colloidal dispersions.

Antioxidant activity test

Our study evaluated ZnO-NPs' ability to eliminate free radicals using a 2,2-diphenyl-1-picrylhydrazyl (DPPH) radical scavenging assay. During the experiment, we observed the color change of a DPPH/methanol solution when it was exposed to NPs. We carried out experiments to evaluate the DPPH radical scavenging activity of pure ZnO NPs, S-doped ZnO NPs, and N-doped ZnO NPs. To do this, we prepared a 0.1 mM DPPH/methanol solution, which normally appears purple or violet but turns yellow in the presence of antioxidants. Next, we mixed it with 1 mL of methanol solution containing each type of nanoparticle at concentrations of 70, 90, 110, and 130 mg/mL. After vortexing and allowing the mixture to stand in the dark at room temperature for 30 min, we used a spectrophotometer to measure the absorbance at 517 nm and calculate the percentage of DPPH radical scavenging activity (Equation 1). Ascorbic acid was used as the standard in this experiment.

$$\% \text{ scavenging activity of DPPH radical} = (A_0\text{-}A_1))/A_0 \text{ X } 100 \quad (1)$$

where A_0 represents the absorbance of the control and A_1 represents the absorbance of the sample. After plotting the percentage of inhibition against concentration, the IC_{50} was determined from the graph. The experiment was carried out three times at each concentration.

Antimicrobial activity

Microbial studies were conducted using the agar disc diffusion method in the Laboratory of the Biology Department at Jimma University [40]. The synthesized nanoparticles were tested for their antibacterial effects against *Staphylococcus aureus*, *Salmonella typhi*, *Bacillus cereus*, and *Escherichia coli*. Additionally, the effectiveness of the antifungal agent was evaluated against *Candida albicans*. The antibacterial action of the manufactured ZnO, GO, and ZnO/GO-NCs against the pathogenic bacterial species was investigated using the agar well diffusion assay [41]. A total of 50 µL of control-test samples were added to 6 mm wells on a nutrient agar plate that had been incubated for 24 hours in a sterile manner. The wells were then sealed and allowed to solidify for 90 min. The turbidity of the bacterial test organism was adjusted using a 0.5 McFarland solution. For the experiment, a negative control was created using DMSO. Gentamicin and clotrimazole were used as positive controls for bacteria and fungi, respectively. To prepare the sample solution, 90 mg/mL of the individual compound being tested was dissolved in DMSO.

Then, bacterial strains were swabbed onto the plates and incubated at 37 °C for 24 hours. The antibacterial activity was determined by measuring the zone of inhibition.

RESULTS AND DISCUSION

Characterization

ZnO nanoparticles and their graphene oxide nanocomposites were characterized using UV-Vis, XRD, FTIR, and SEM instruments. ZnO/GO nanocomposites were obtained by sonication. The optical properties and light absorption features of the pristine ZnO-NPs and its GO nanocomposites were recorded using UV-Vis spectrophotometer. According to Figure 2, the UV-Vis absorbance peak of the ZnO/GO-NCS was shifted towards low energy wavenumber compared to the pure ZnO-NPs. A maximum shift was also achieved by optimizing the amount (percentage) of the GO required. Accordingly, adding 4% (wt/wt) GO to pure ZnO-NPs caused the absorbance peak to shift from 371 nm to 378 nm. Surface charge enhancement and crystallinity of the NPs cause this change. UV-Vis spectroscopic studies (Figure 2a) reveal that the dominant optical absorption of GO occurs at 239 nm. The chromophore unit is C=C and belongs to a plasmon peak of sp^2 clusters at nm scale. The peak at approximately 300 nm corresponds to an n-$\pi*$ plasmon peak of carboxyl, other carbonyl and hydroxyl (C=O) auxochromes. Figure 2b shows the UV-Vis absorption spectra of small amounts of GO doped ZnO, from which it can be seen that the samples have strong absorption at 378 nm, corresponding to the intrinsic band width of ZnO-NPs.

The addition of GO to ZnO photocatalysts has altered their light absorption properties, causing a significant shift in their absorption intensity into the visible range and reducing their bandgap. To determine the samples' bandgap energies, we calculated the values of α, $h\nu$, and $(\alpha h\nu)^2$ from the UV-Vis data. Figure 2 illustrates the relationship between $(\alpha h\nu)^2$ and photon energy (hν) for both ZnO nanoparticles (NPs) and ZnO/GO nanocomposites (NCs). Upon the integration of GO into pristine ZnO-NPs, the optical bandgap of ZnO-NPs decreased from 2.87 eV (as shown in Figure 2c) to 2.20 eV (as depicted in Figure 2e). The reduction in the energy band gap can be attributed to the influence of GO on the surface charge and stability of the nanomaterial.

The XRD analysis has provided information on the phases and structures of ZnO, GO, and ZnO/GO-NCs (JCPDS card No. 5.0664). The purpose of the XRD measurements was to investigate the crystal structure of ZnO and ZnO/GO under different preparation conditions. The measurements have shown characteristic peaks at 2θ = 29º, 31.7°, 34.4°, 36.2°, 47.5°, 56.7°, 63.0°, 68.1°, and 69.3° for ZnO and ZnO/GO-NCs annealed at 350 °C (Figure 3). These peaks correspond to the planes (100), (002), (101), (102), (110), (103), (200), and (112), respectively. [10, 42-44].

It was determined that ZnO was present in the hexagonal wurtzite phase, with no other phases or impurities detected [42]. There were no characteristic peaks of any impurities found, indicating that no pure GO was present in the XRD pattern of ZnO/GO. This may be due to limited amounts of GO covering the ZnO crystals, which altered its structure [45]. The presence of amorphous superficial and intergranular layers between ZnO and ZnO/GO photocatalysts confirms the existence of grain boundaries in ZnO and ZnO/GO-NCs, which were not observable in XRD patterns.

The crystallite sizes of the pristine and GO integrated ZnO nanoparticles have been obtained from the full width at half maximum (FWHM) of the most intense peaks of the respective crystals using the Scherrer equation (Equation 2). Based on this equation, the calculated the average particle size calculated from the XRD data for the pristine ZnO-NPs and ZnO/GO nanocomposite were found to be 37.20 nm and 32.44 nm respectively. This the integration of the GO into ZnO nanoparticles reduced its particle size indicating its relative stability.

$$D = 0.9\lambda/\beta\cos\theta \quad (2)$$

where λ is the X-ray wavelength, D the average crystallite size, θ the Bragg diffraction angle and β the FWHM in radians.

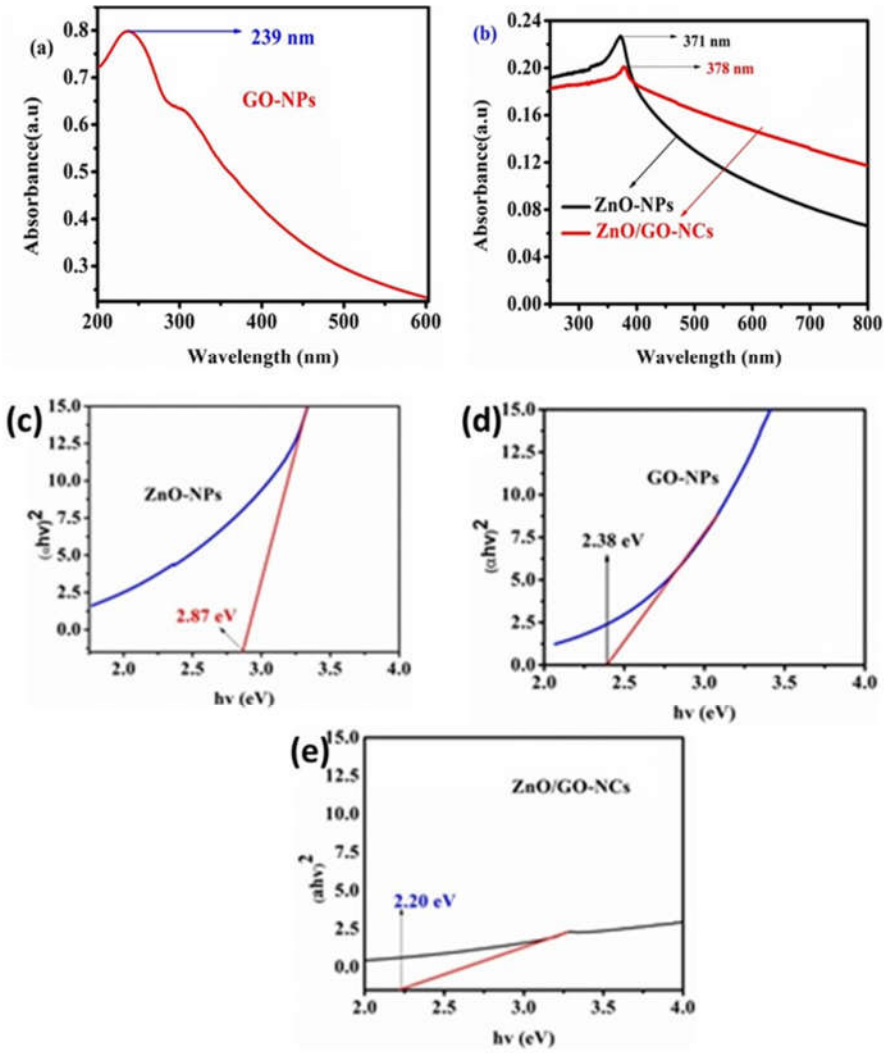

Figure 2. UV-Vis spectrum of (a) GO-NPs, (b) ZnO-NPs (black) and ZnO/GO (red) NCs and energy bandgaps of (c) ZnO-NPs, (d) GO-NPs and (e) ZnO/GO-NCs.

FT-IR measurements were conducted on the synthesized GO, ZnO-NCs, and ZnO/GO-NC to compare the chemical structure of the moieties attached to their surfaces. The analysis was conducted by comparing them with pure ZnO-NPs, as shown in Figure 3c. The FT-IR spectral bands of the nanomaterials were observed within the wavenumber range of 4000-400 cm^{-1}. The FT-IR peaks of GO, displayed in Figure 3c, were found at 570, 1000, 1170, 1620, 1735, and 3400 cm^{-1}. The peak at 1000 cm^{-1} was linked to C-O vibrations of the graphitic domains [46, 47]. A

peak at 1170 cm^{-1} was attributed to the C-OH group. The presence of C=C and C=O groups in the carboxylic acid was evident from peaks observed at 1620 cm^{-1} and 1735 cm^{-1}, respectively. The peak at 3400 cm^{-1} was due to O-H groups present in the water absorbed by GO from the air. The new broad peak at 650 cm^{-1} in ZnO/GO-NCs, as shown in Figure 3c, is associated with Zn-O vibrations, supplementing the identified peaks shared by ZnO/GO-NCs and GO [47].

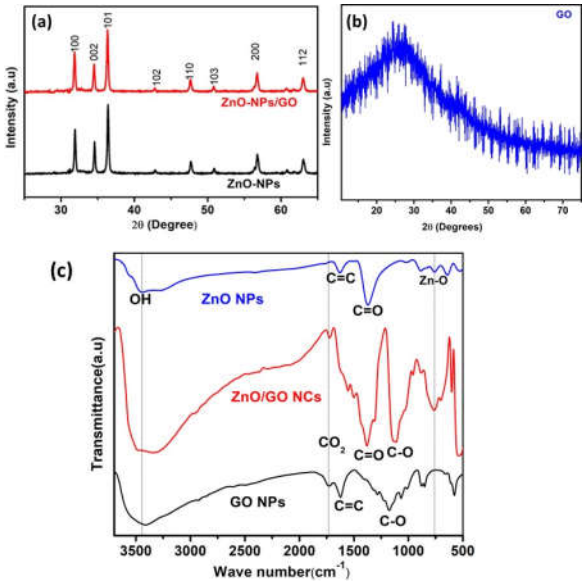

Figure 3. The XRD patterns and FTIR spectrum of (a) pristine ZnO-NP (black) and ZnO/GO (red) nanocomposite and (b) GO (blue) (c) FTIR spectrum for GONPs, ZnO/GO-NCs and pure ZnONPs.

According to the vibrations observed, graphene oxide (GO) sheets are attached to ZnO particles. The hydrogen bonds between graphite and H_2O molecules make GO hydrophilic, as shown by the wide peak at 3400 cm^{-1}. The OH groups of water molecules on GO, along with polar groups, especially the surface hydroxyl groups, contribute to this characteristic. Absorption bands at 2481 cm^{-1} and 1744 cm^{-1} correspond to C-H, C=O, and C=C bond stretching vibrations. Additionally, stretching vibrations of alcohol and carboxylic acids can also be observed at 1170 cm^{-1} and 1350 cm^{-1}, respectively. Graphite that contains oxygen-containing groups has been oxidized. According to the FTIR spectrum of GO, graphite has been successfully oxidized. The GO diffraction peak in the composite is not distinct due to its low content and amorphous nature. However, the peaks of the composites are similar to those of ZnO-NPs, suggesting that GO modification does not significantly alter the crystallinity of ZnO.

The micrographs of synthesized ZnO, GO, and their composites were captured using SEM and are presented in Figure 4. The surface of GO appeared smooth, wavy, and textured. The ZnO-NPs sample exhibited spherical structures formed by the agglomeration of ZnO-NPs. The SEM image of GO showed a stacked GO sheet morphology with severe agglomeration due to its high specific surface area. GO had a layered structure primarily consisting of carbon and oxygen in similar proportions. Figure 4a illustrates ZnO-NPs forming agglomerations. The morphology of the ZnO/GO-NCs sample in Figure 4c showed less agglomeration of ZnO-NPs with some rod-like structures of ZnO, possibly due to their dispersion in the GO suspension.

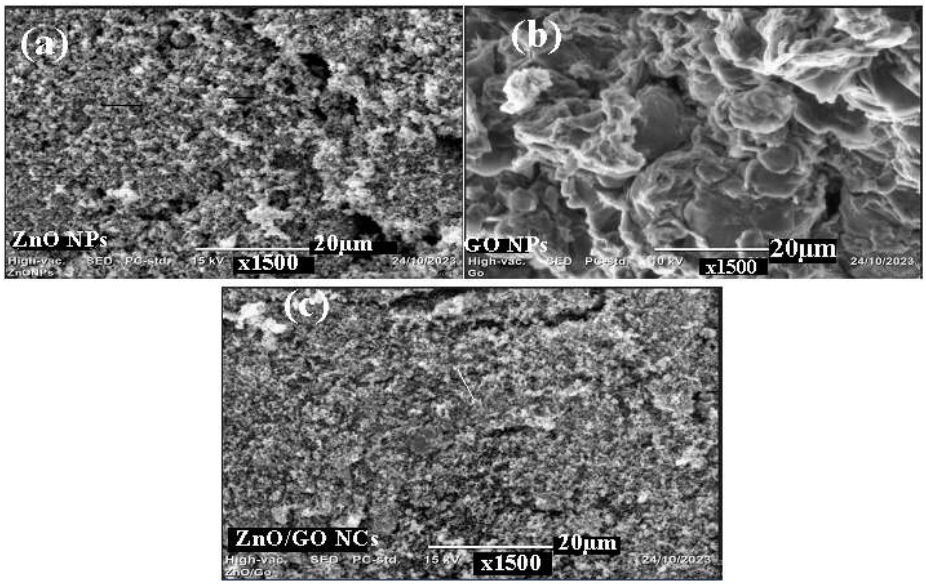

Figure 4. The SEM images of: a) ZnO NPs, b) GO NPs, and c) ZnO/GO NCs.

Photocatalytic synthesis of photocatalysts involved decomposing Methylene Blue (MB) with optical absorption spectroscopy. The efficiency of a semiconductor photocatalyst like ZnO strongly depends on its electronic structure. Photogenerated holes (h^+) in the valence band (VB) and electrons (e-) in the conduction band (CB) of the photocatalyst initiate the degradation of organic compounds in solution. The resulting h^+ has high oxidative potential, enabling direct oxidation of organic compounds to reactive intermediates. Hydroxyl radicals also play a role in degrading the organic substrate. NP doping can reduce the recombination of excited electrons in the CB with holes in the VB, enhancing oxy radical's production by reacting with oxygen molecules and promoting oxidative degradation of MB molecules.

To assess photocatalyst performance, pure ZnO semiconductors and ZnO/GO-NCs from different preparation methods were used to degrade model pollutants and MB. Decomposition of MB dye was studied with ZnO/GO-NCs produced from ZnO-NPs and GO-NPs, exposed to sunlight in Jimma at intervals of 0, 10, 20, 30, 40, 50, 60, 70, and 80 minutes. Color changes in the solution from blue to colorless indicate that the characteristic MB absorption peak at 666 nm diminishes with dye degradation.

Parameter optimization for photocatalytic dye degradation

The optimal conditions for the maximum degradation (%) and the minimum final concentration of dye were determined to be light intensity, initial dye concentration, catalyst dose, point of zero charge, and the effect of pH. The following factors were identified prior to conducting the photocatalytic test, as shown in Figure 5.

Effect of catalytic dosage

Photocatalyst concentration significantly impacts degradation efficiency. Results in Figure 7(a) show that increasing catalyst dosage from 10 mg/mL to 20 mg/mL enhances MB dye degradation efficiency from 91% to 98%. Higher photocatalyst concentrations boost absorbance of light and generate more charge carriers, reaching peak photocatalytic activity at an optimal dosage. However, beyond 20 mg/mL, MB photocatalytic activity decreases due to solution turbidity hindering light penetration. Experiments varied ZnO/GO photocatalyst concentrations (10 mg, 20 mg, 30 mg) at constant MB dye levels (10 ppm) to determine optimal levels. The nanocomposite offers increased adsorption sites and surface area under sunlight, promoting hydroxyl free radical production for enhanced contact with MB dye pollutants.

Catalyst loading at 10 mg/mL, 20 mg/mL, and 30 mg/mL resulted in 91%, 98%, and 81.12% degradation, respectively. The initial increase in yield suggests an increase in active sites on the surface of ZnO/GO due to a higher dosage.

In our experiment, we observed that the absorbance of MB under ultraviolet and visible light from a high-pressure mercury lamp decreased over time, as shown in Figure 5(a). This confirmed that ZnO/GO-NCs effectively degraded MB. We also noted that as the suspension became more turbid, it hindered the photocatalytic process and reduced light penetration. Additionally, we found that increasing the amount of catalyst from 10 to 20 mg led to higher photocatalytic activity, likely due to the presence of more active sites. However, when the catalyst amount exceeded 20 mg, the activity decreased. This decrease was possibly due to light scattering and screening effects caused by particle aggregation, which hindered light irradiation. Figure 5(a) illustrates that MB degradation increased from 81.12% to 98% as the dosage of ZnO/GO-NCs changed from 10 mg to 30 mg. However, it is important to note that there was no significant improvement in MB degradation with doses exceeding 20 mg. Therefore, a 20 mg catalyst dosage was considered optimal for degrading 10 ppm MB. Figure 5(b) illustrates real-time MB concentration changes with increasing irradiation time for all catalysts under UV and visible light. In the absence of ZnO or ZnO/GO-NCs, minimal MB degradation occurred under UV light, indicating MB's relative stability without a catalyst. Similarly, without photocatalysts, there was nearly no MB photodegradation under visible light. The subsequent decline in degradation efficiency with increased catalyst dosage beyond the optimum can be attributed to suspended particle accumulation inhibiting light access to active sites, thereby reducing reaction rates. The incorporation of GO can enhance dye adsorption and facilitate ZnO carrier separation effectively.

Point of zero charge

Determining the point of zero charge (pHPZC) is crucial for predicting the nanoparticle surface charge during the photocatalytic degradation of pollutants. In the photocatalytic process involving ZnO/GO-NCs, the isoelectric point (PZC) is reached when the net charge of the particles becomes zero at a specific pH. pH pzc data of the adsorbents provides insight into the interaction between catalyst and MB dyes. In environmental science, it indicates the substrate's ability to adsorb harmful ions. pH also affects the ionization of active sites on the sorbent. The pH of point zero charge (PZC) is the pH where surface charge components balance under specific conditions. This doesn't mean no charge at the surface, but equal negative and positive charges. During photocatalysis, the point of zero charge (PZC) of nanocrystals indicates the variable-charged surface of the catalyst. This study determined the PZC of ZnO/GO-NCs to be in the pH range of 6 to 12 (PZC at 7.5). Above this pH, the surface is negatively charged, favoring positively charged particle adsorption. Below PZC, negatively charged dyes are preferred, repelled by negatively charged surfaces. Adjusting the photocatalytic system's pH can modify the surface charge for selective dye degradation. For MB dye, a cationic dye, a pH above PZC is ideal for decomposition due to the presence of exchangeable OH- (Figure 5c).

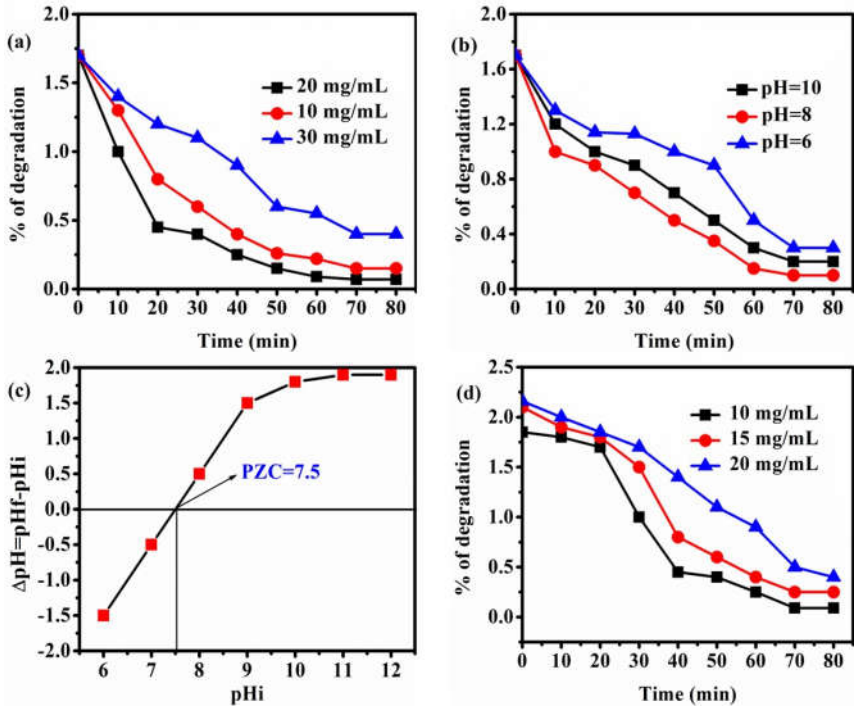

Figure 5. Degradation competence of MB dye on a) the catalyst dosage, b) the solution pH, c) the point of zero charge, and d) the optimization of initial MB concentration.

Effect of pH

The rate at which a dye is degraded and adsorbed is influenced by the degree of acidity and basicity of the medium [48]. In a photocatalytic system, the rate of degradation depends on the pH level and the dye's ability to adhere to the photocatalyst. When more target molecules stick to the catalyst, the degradation rate increases. In order to investigate how pH affects the degradation of MB and its adsorption capacity, we adjusted the pH of the MB solution to 6, 8, and 10 using 0.1M HCl and 0.2M NaOH solutions. We used 20 mg of catalyst and a 10 ppm dye concentration for 80 minutes. In Figure 5b, you can observe the percentage of MB degradation at different pH levels.

According to this study, the photocatalytic activity of MB dye on ZnO/GO-NCs increases as the pH level rises, reaching its highest efficiency at pH 8. However, this limits the effectiveness of the nanocatalysts and prevents the generation of free radicals on the photocatalyst's surface when exposed to sunlight. The maximum removal of methylene blue dye was achieved after 80 minutes, reaching 98% when ZnO/GO was introduced at pH 8, which is close to the solution's pH pzc value.

Effect of initial dye concentration

The initial dye concentration plays a crucial role in the adsorption process, impacting the efficiency of dye removal by influencing the availability of binding sites on the adsorbent surface.

Higher adsorption capacity is observed at lower concentrations due to the increased availability of active sites for dye molecules to attach to the photocatalyst's surface. The percentage of degradation decreases with higher initial concentrations of organic pollutants (from 10-20 mg/mL of dye, dropping from 21% to 17.12%). This decrease can be attributed to the rise in dye sorbate on the surface-active sites of the photocatalyst, limiting the adsorption of OH- and reducing the formation of highly oxidative OH* radicals. Moreover, higher dye concentrations hinder visible light penetration on the active sites of the photocatalyst, thus diminishing its activity. In the experiment, the researchers tested different concentrations of dye (ranging from 10-20 mg/mL) to determine the best dosage for optimum performance. They discovered that the nanoparticles had higher photocatalytic activity when the dye concentration was lower (10 mg/mL), but their efficiency decreased as the concentration of dye increased. This was because an increase in the amount of dye molecules adsorbed on the catalyst surface resulted in a decrease in the photodegradation process. This increased adsorption of dye molecules on the surface-active sites of the photocatalyst results in fewer photons reaching the catalyst surface, reduced OH^- adsorption, and subsequently lower production of highly oxidative, $OH^{\cdot}$ radicals. The efficiency of degrading MB dye decreased as the concentration of the dye increased. The best efficiency of 98% was achieved when ZnO/GO-NCs were used at a pH of 8 with a concentration of 10 mg/mL of MB. After 80 minutes, the photo degradation rates for 10, 15, and 20 mg/mL of MB dye were found to be 21.7%, 18.3%, and 17.12% respectively (Figure 5).

Effect of contact time

The exceptional properties of metal/semiconductor nanocrystal photocatalysts arise from the improved separation of charges at the metal-semiconductor interface and the enhanced absorption of visible light due to the surface plasmon resonance of metals. The efficiency of the prepared ZnO nanoparticles and graphene oxide nanocrystals was evaluated by decomposing methylene blue (MB) dye.

The degradation of MB dye was monitored using UV-Vis absorbance spectra under varying exposure durations. The absorbance levels were measured to calculate the degradation percentage. For the experiment, a 50 mL sample containing 10 mg/L dye at pH 8 was placed in a volumetric flask. Subsequently, 20 mg of the photocatalyst was added, and the mixture was continuously agitated for 0, 10, 20, 30, 40, 50, 60, 70, and 80 min while being exposed to light. The UV-Vis absorption levels of ZnO-NPs with MB, ZnO/GO with MB, and pure MB were measured every 10 min. As shown in Figure 6, the degradation kinetics of MB can be observed in UV-Vis absorption profiles. The pure ZnO-NPs mixed with MB showed a gradual decrease in absorption peaks (Figure 6a) when exposed to light. According to UV-Vis examination, the peak intensity of the ZnO/GO mixture with MB meaningfully decreased, almost reaching zero after 80 minutes of light exposure (Figure 6b). As the intensity of the absorbance peak decreased, the solution's color faded and eventually turned colorless after 80 minutes of light exposure (Figure 6d). The nanocomposite achieved the highest MB dye degradation efficiency, with 98% degradation occurring within 80 min. Conversely, MB without the catalyst exhibited minimal degradation under light exposure, with peak intensities largely unchanged after 80 min. Figure 6 demonstrates that without a photocatalyst, no degradation of MB was observed even after 80 minutes of visible light exposure, indicating the high stability of MBs [50]. A highly efficient ZnO/GO-NCs photocatalyst was synthesized through a chemical approach utilizing GO and ZnO for the photodegradation of MB dye. The photocatalytic mechanism involves light irradiation with adequate energy to match or exceed the semiconductor's band-gap, leading to the excitation of an electron from the valence band (VB) to the conduction band (CB) as indicated in Scheme 1. We developed a ZnO NPs-decorated with GO to form ZnO/GO nanocomposite that improves surface-charge, surface-area, and shifts the bandgap to the red spectrum as a photocatalyst for organic dye degradation.

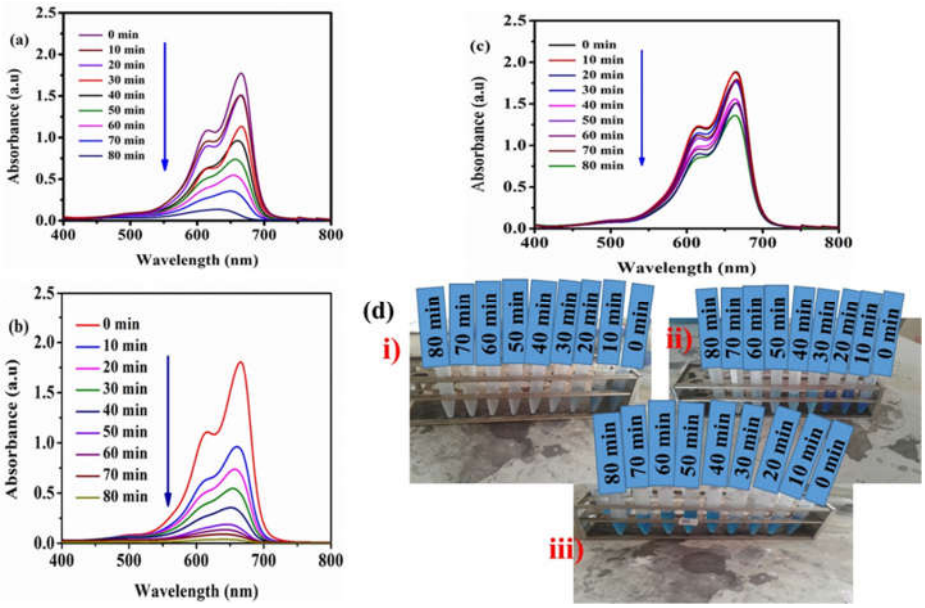

Figure 6. UV-Vis absorption spectrum for the degradation kinetics of MB dye on: a) pristine ZnO-NPs, b) ZnO/GO-NCs, c) MB dye on sunlight, d) MB dye at diverse removal stages with i) ZnO/GO-NCs, ii) ZnO-NPs, and iii) Dye without catalyst.

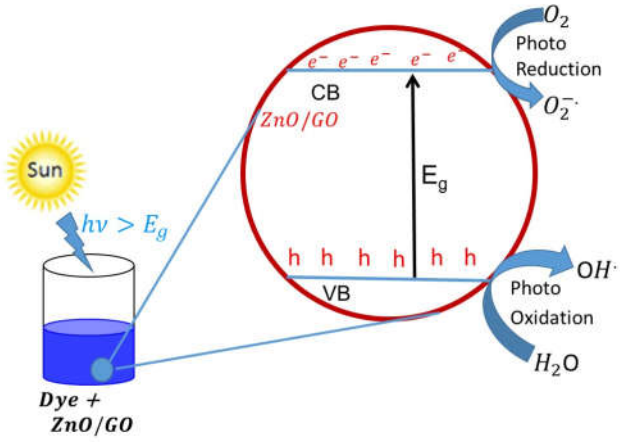

Scheme 1. Mechanism of the photocatalytic reduction of MB dye.

The ability of ZnO/GO-NCs to be used repeatedly for dye decomposition was tested over three MB degradation cycles. After each cycle, the photocatalyst was rinsed with ethanol and reused. Figure 7 illustrates the recycling process of the ZnO/GO-NCs photocatalyst. The same optimal parameters were used to evaluate the reusability. The degradation efficiencies for the first, second, and third cycles were 98%, 93.02%, and 86.10%, respectively. The initial dye concentration was

10 mg/L with a catalyst dose of 20 mg, pH 8, and 80 min of irradiation. However, the efficiency of the ZnO/GO-NCs photocatalyst decreased in subsequent cycles, likely due to the build-up of waste ions and impurities from the catalyst. Nevertheless, the study shows that the synthesized ZnO/GO-NCs photocatalyst can be reused for three consecutive cycles with only a slight efficiency decrease, indicating its stability and effectiveness.

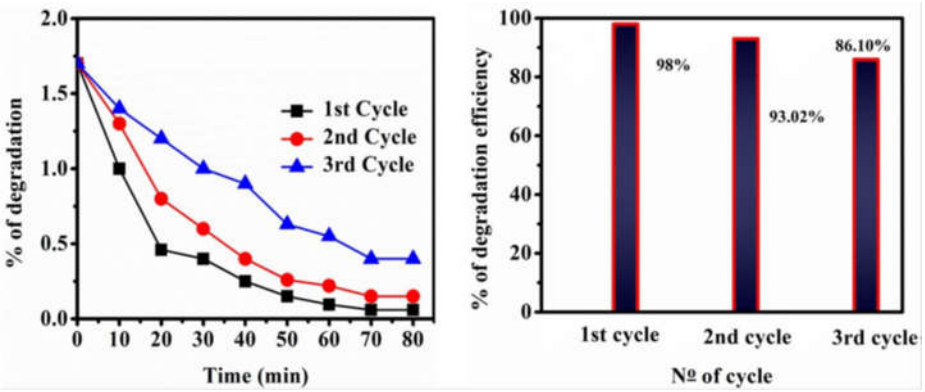

Figure 7. Recyclability test conducted to check catalytic nature of ZnO/GO-NCs.

Radical scavenging activity

Radical scavenging activity is involved in ageing processes, anti-inflammatory, anticancer and wound healing activity. Hence, in the present study the DPPH radical scavenging activity of a natural product that possesses biological properties. The activity of scavenging DPPH radical was calculated by the following Equation (3):

$$\text{Scavenging activity (\%)} = ((Ac\text{-}As)*100)/Ac \quad (3)$$

In this equation, Ac is the absorbance of the control, while As is the absorbance of the sample.

The NCs, ZnO, and ZnO/GO were tested for their antioxidant properties by conducting DPPH radical scavenging assays. In Figure 8, it is observed that the ability to scavenge the DPPH radical increases as the concentration of the tested samples ranges from 5 to 80 µg/mL. The DPPH radical scavenging activity of different samples and ascorbic acid at 80 µg/mL follows the order: Ascorbic acid (98.8%) > ZnO/GO, 80 µg/mL (51.6%) > ZnO/GO, 40 µg/mL (49%) > ZnO/GO, 20 µg/mL (44.12%) > ZnO/GO, 10 µg/mL (39.1%) > ZnO/GO, 5 µg/mL (38.5%). The DPPH RSA method of ZnO NPs is in the order of ascorbic acid (98.8%) > ZnO, 80 µg/mL (38.38%) > ZnO, 40 µg/mL (34.19%) > ZnO, 20 µg/mL (31.6%) > ZnO, 10 µg/mL (30.36%) and ZnO, 5 µg/mL (23.8%). This method is based on the reduction of DPPH, which is a stable free radical.

This research indicates that ZnO/GO-NCs can prevent oxidation by transferring the electron density of oxygen to carbon in DPPH free radicals through n→π* transition (Scheme 2). The antioxidant abilities of ZnO-NPs and ZnO/GO were tested using the DPPH method, which showed an increase in radical scavenging effectiveness with higher concentrations of NPs. The half-maximal inhibitory concentrations (IC50) for the NPs were 38.38% for ZnO-NPs and 51.6% for ZnO/GO-NCs, indicating their different radical scavenging effectiveness. The synthesized NPs were also tested against DPPH where ZnO-NPs showed significant antioxidant activity, while ZnO/GO demonstrated inhibition at 50 µg/mL. This suggests that ZnO/GO can hinder oxidation by transferring electron density from oxygen to carbon in the DPPH free radical through a transition. [24, 49]. Antioxidants can reduce oxidative damage by directly interacting with free

radicals or indirectly by inhibiting the activity or expression of free radical-generating enzymes, or by boosting the activity or expression of intracellular antioxidant enzymes.

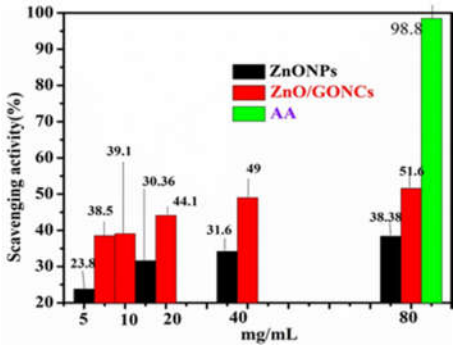

Figure 8. DPPH Radical Scavenging Activity of ZnO and ZnO/GO-NCs Values labelled on the top of the columns in the histogram correspond to anti- oxidant activity of each sample from 5 µg/mL through 80 µg/mL.

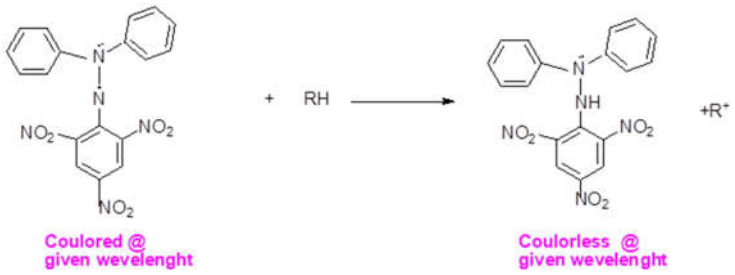

Scheme 2. The radical scavenging mechanism of DPPH.

Antimicrobial activity

The antimicrobial effects of three synthesized nanoparticles (NPs)-ZnO-NPs, GO-NPs, and ZnO/GO-NCs - were examined against both Gram-positive and Gram-negative bacteria using the disk diffusion method (Figure 9). Positive and negative controls were included in the form of gentamicin and DMSO, respectively. The NPs were tested on five bacterial strains: *S. aureus*, *E. coli*, *B. cereus*, *C. alb*, and *S. typhie* at varying concentrations (30, 60, and 90 mg/mL). The results show that the gram-negative bacteria such as *S. aureus* and *B. cereus* are more susceptible to ZnO-NPs while the gram-positive bacteria like *E. coli* and *S. typhie* are more susceptible to ZnO/GO-NCs.

The nanoparticles (NPs) released zinc ions that adhered to the negatively charged bacterial cell wall. This led to the breakdown of the cell wall, alteration of proteins, and ultimately, the death of the cell. Smaller NPs were more effective at penetrating the cells, leading to faster damage compared to larger particles. A higher concentration of NPs resulted in enhanced bacteria-killing ability, which aligns with findings from other studies. The material containing a mix of nanoparticles demonstrated superior bacteria-killing capabilities compared to zinc oxide ZnO-NPs and GO on their own. This indicates that the inclusion of GO-NPs improved the material's bacteria-killing effectiveness.

The results in Table 1 show that gram-positive bacteria, specifically *S. aureus* and *B. cereus*, were highly susceptible to the synthesized ZnO-NPs and ZnO/GO-NCs, while gram-negative strains like *E. coli* and *S. typhie* were less affected. The inhibition zones for *S. aureus* and *B. cereus* were 17 mm and 20 mm, respectively, for the composite, while for *E. coli* and *S. typhie*, they were 14 mm and 15 mm, respectively. GO is known for its antibacterial properties and is widely used in commercial product packaging and various biomedical applications. It inhibits bacterial growth by depriving them of essential nutrients, ultimately causing cell death. For more details on the antimicrobial inhibition zones, check Table 1.

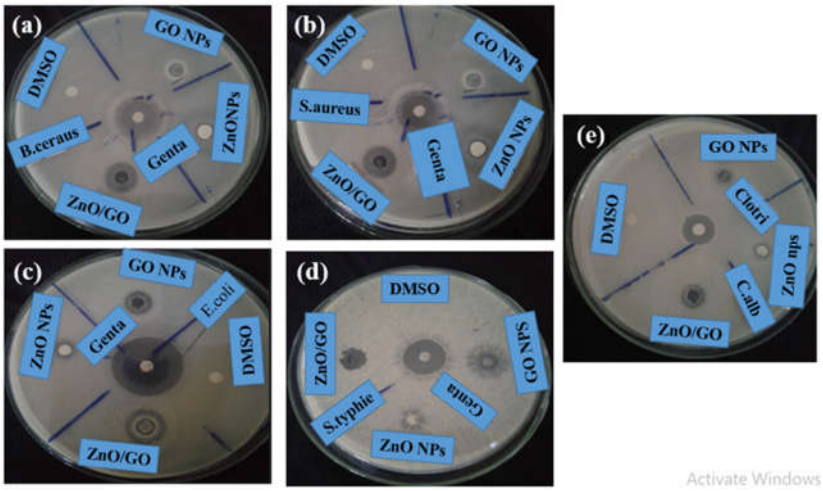

Figure 9. Antimicrobial activity of ZnO-NPs, GO-NPs, and ZnO/GO-NCs on (a) *B. ceseus*, (b) *E. coli* , (c) *S. aureus*, (d) *S. Typhis* and (e) *C. alb*.

Table 1. Anti-microbial Activities of ZnO-NPs, GO-NPs and their composites.

Micro organisms	Zone of inhibition (mm)				
	Controls		Materials (90 mg/mL)		
	Gentamicin (+ve)	DMSO (-ve)	ZnO NPs	GO NPs	ZnO/GO NCs
B. seraus	24	0	10	12	17
S. aureus	24	0	10	13	20
S. typhie	23	0	10	11	14
E. coli	22	0	8	11	15
C. alb	24	0	8	12	15

CONCLUSION

We successfully prepared high-quality ZnO/GO-NCs by mixing ZnO and GO solutions using the sol-gel method with aqueous precursor solutions. The crystal structure, band gap energy, bond vibration properties, and morphologies of ZnO nanoparticles and ZnO/GO-NCs were analyzed using XR), double-beam UV-Vis, FT-IR, and SEM) Adding GO to ZnO-NPs enhanced their surface charge and uniformity, reducing the energy band gap of ZnO-NPs from 2.87 eV to 2.20 eV. The synthesized ZnO/GO-NC materials showed excellent photocatalytic activity on MB dyes under visible light, making it a promising candidate for photocatalytic waste water treatment. The

ZnO/GO-NCs photocatalyst effectively decolorized MB dye under direct solar irradiation, and the addition of GO materials improved the surface charges of the nanocomposites, enhancing photocatalytic degradation efficiency. Through comprehensive characterization methods such as XRD, we confirmed that the particle size appreciably decreased due to the improved stability. The photocatalytic degradation efficiency of ZnO/GO surpassed that of pure ZnO-NPs due to improved surface charge, with ZnO/GO prepared at pH 8 achieving an optimal efficiency of 98.4% degradation. ZnO, GO, and various concentrations of ZnO/GO-NCs were synthesized and characterized, demonstrating good antibacterial activity against pathogenic microorganisms. The antioxidant activity of the materials has also improved as the result of GO incorporation. Overall, the results indicate that the integration of GO into ZnO-NPs enhanced various activities the pure ZnO-NPs.

ACKNOWLEDGEMENT

This work was financially supported by the College of Natural Sciences at Jimma University under the PG student project.

Conflict of interest

The authors declare that they have no known competing financial interests or personal relationships that could have appeared to influence the work reported in this paper.

Availability of data and materials

Data available on request from the authors.

REFERENCES

1. Lellis, B.; Favaro-Polonio, C.Z.; Pamphile, J.A.; Polonio, J.C. Effects of textile dyes on health and the environment and bioremediation potential of living organisms. *Biotechnol. Res. Innov.* **2019**, 3, 275-290.
2. Garg, A.; Lalita, C. Dye waste: A significant environmental hazard. *Mater. Today Proc.* **2022**, 48, 1310-1315.
3. Rania, A.T.; Sameh, S.A.; Fanghua, L; Kamal, M.O.; Yehia A.G.M.; Tamer, E.; Haixin, J.; Yinyi, F.; Jianzhong, S. A critical review on the treatment of dye-containing wastewater: Ecotoxicological and health concerns of textile dyes and possible remediation approaches for environmental safety. *Ecotoxicol. Environ. Saf.* **2022**. 231, 113160.
4. Jiuyang, L.; Wenyuan, Y; Ming, X., Dong, H.S.; Jianquan, L.; Yinhua, W.; Bart, V.B. Environmental impacts and remediation of dye-containing wastewater. *Nat. Rev. Earth Environ.* **2023**, 4, 785-803.
5. Giusy, T; Gioconda, B.; Daniele, R.G.; Alberto, E.M.; Floriana, G.; Marco, F.; Maddalena, G.; Paolo, G.; Federico, P.; GianMaria, R.; Maurizio, S.; Mario, S.; Claudio, S.; Mario, T.; Mario, V.; Pierluigi, V.; Matteo, B.; Francesco, L; Francesco, M.; Stefania, S.; Marco, T. Diagnosis and management of infections caused by multidrug-resistant bacteria: Guideline endorsed by the Italian Society of Infection and Tropical Diseases (SIMIT), the Italian Society of Anti-Infective Therapy (SITA), the Italian Group for Antimicrobial Stewardship (GISA), the Italian Association of Clinical Microbiologists (AMCLI) and the Italian Society of Microbiology (SIM). *Int. J. Antimicrob. Agents* **2022**, 60, 106611.
6. Gajic, I.; Jovicevic, M.; Popadic, V.; Trudic, A.; Kabic, J.; Kekic, D.; Ilic, A.; Klasnja, S.; Hadnadjev, M.; Popadic, D.J.; Andrijevic, A.; Prokic, A.; Tomasevic, R.; Ranin, L.;

Zdravkovic, M.; Opavski, N. The emergence of multi-drug-resistant bacteria causing healthcare-associated infections in COVID-19 patients: a retrospective multi-centre study. *J. Hosp. Infect.* **2023**, 137, 1-7.
7. Lee, N.Y.; Ko, W.C.; Hsueh, P.R. Nanoparticles in the treatment of infections caused by multidrug-resistant organisms. *Front. Pharmacol.* **2019**, 10, 1153.
8. Sahba, E.; Farhad, M.; Mahmoud, R.H. Recent advance on nanoparticles or nanomaterials with anti-multidrug resistant bacteria and anti-bacterial biofilm properties: A systematic review. *Heliyon* **2023**, 9, e22105.
9. Tegenaw, A.B.; Yimer, A.A.; Beyene, T.T. Boosting the photocatalytic activity of ZnO-NPs through the incorporation of C-dot and preparation of nanocomposite materials. *Heliyon* **2023**, 9, e20717.
10. Aga, K.W.; Efa, M.T.; Beyene, T.T. Effects of sulfur doping and temperature on the energy bandgap of ZnO nanoparticles and their antibacterial activities. *ACS Omega* **2022**, 7, 10796-10803.
11. Etefa, H.F.; Nemera, D.T.; Etefa, J.; Ranjith, K.E. Evaluation of physicochemical properties of zinc oxide and indium-tin oxide nanoparticles for photocatalysis and biomedical activities. *Curr. Appl. Phys.* **2024**, 67, 133-142.
12. Kaur, D.; Bharti, A.; Sharma, T.; Madhu, C. Dielectric properties of ZnO-based nanocomposites and their potential applications. *Int. J. Opt.* **2021**, 2021, 1-20.
13. Xian-Qing, Z.; Xian-Qing, Z.; Zakir, H.; Dong-Dong, Z.; Meng-Yao, L.; Si, H.; Wu, Q.; Ca, Y.; Yuan, Y. Zinc oxide nanoparticles: Synthesis, characterization, modification, and applications in food and agriculture. *Processes* **2023**, 11, 1193.
14. Pushpalatha, C.; Suresh, J.; Gayathri, V.S.; Sowmya, S.V.; Dominic, A.; Ahmed, A.; Bassam, Z.; Nassreen, Hassan, M.A.; Shankargouda, P. Zinc oxide nanoparticles: A review on its applications in dentistry. *Front. Bioeng. Biotechnol.* **2022**, 10, 917990.
15. Gudkov, S.V.; Burmistrov, D.E.; Serov, D.A.; Rebezov, M.B.; Semenov, A.A.; Lisitsyn, A.B. A mini review of antibacterial properties of ZnO nanoparticles. *Front. Phys.* **2021**, 9. 641481.
16. Jiang, J.; Pi, J.; Cai, J. The advancing of zinc oxide nanoparticles for biomedical applications. *Bioinorg. Chem. Appl.* **2018**, 2018, 1062562.
17. Rahman, H.S.; Othman, H.H.; Abdullah, R.; Yahya, H.; Edin, A.S.; AL-Haj, N.A. Beneficial and toxicological aspects of zinc oxide nanoparticles in animals. *Vet. Med. Sci.* **2022**, 8, 1769-1779.
18. Jiang, J.; Pi, J.; Cai, J. The advancing of zinc oxide nanoparticles for biomedical applications. *Bioinorg. Chem. Appl.* **2018**, 2018, 1062562.
19. Smaoui, S.; Cherif, I.; Hlima, H.B.; Khan, M.U.; Rebezov, M.; Thiruvengadam, M.; Sarkarj, T.; Shariati, M,A.; Lorenzo, J.M. Zinc oxide nanoparticles in meat packaging: A systematic review of recent literature. *Food Packag. Shelf.* **2023**, 36, 101045.
20. Davis, K.; Yarbrough, R.; Froeschle, M.; White J.; Rathnayake, H. Band gap engineered zinc oxide nanostructures via a sol–gel synthesis of solvent driven shape-controlled crystal growth. *RSC Adv.* **2019**, 9, 14638-14648.
21. Fiedler, S.; LeeCheong Lem, L.O.; Ton-That, C.; Schleuning, M.; Hofmann, A.; Phillips, M.R. Correlative study of enhanced excitonic emission in ZnO coated with Al nanoparticles using electron and laser excitation. *Sci. Rep.* **2020**, 10, 2553.
22. Talam, S., Karumuri, S.R.; Gunnam, N. Synthesis, characterization, and spectroscopic properties of ZnO nanoparticles. *ISRN Nanotechnology* **2012**, 2012, 372505.
23. Hamada, A.M.; Radi, A.A.; Al-Kahtany, F.A.; Farghaly, F.A. A review: Zinc oxide nanoparticles: Advantages and disadvantages. *J. Plant Nutr.* **2023**, 47, 1-24.
24. Yadesa, D.; Guyasa, J.N.; Beyene, T.T. Effect of codoping zinc oxide nanoparticles with sulfur and nitrogen on its energy bandgap, antioxidant properties, and antibacterial activity. *Adv. Mater. Sci. Eng.* **2024**, 2024, 4275035.

25. Supin, K.K.; Parvathy Namboothiri, P.M.; Vasundhara Vasundhara, M. Enhanced photocatalytic activity in ZnO nanoparticles developed using novel *Lepidagathis ananthapuramensis* leaf extract. *RSC Adv.* **2023**, 13, 1497-1515.
26. Mourya, A.; Singh, R.P.; Kumar, T.; Talmale, A.; Gaikwad, G.S.; Atul V. Wankhade, A.V. Tuning the morphologies of ZnO for enhanced photocatalytic activity. *Inorg. Chem. Commun.* **2023**, 154, 110850.
27. Bansal, K.; Singh, J.; Dhaliwal, A.S. Synthesis and characterization of graphene oxide and its reduction with different reducing agents. *IOP Conf. Ser. Mater. Sci. Eng.* **2022**, 1225, 012050.
28. Jirícková, A.; Jankovský, O.; Sofer, Z.; Sedmidubský, D. Synthesis and applications of graphene oxide. *Materials* **2022**, 15, 920.
29. Tene, T.; Guevara, M.; Palacios, F.B.; Morocho Barrionuevo, T.P. Gomez, C.V.; Bellucci, S. Optical properties of graphene oxide. *Front. Chem.* **2023**, 11, 1214072.
30. Castelletto, S.; Boretti, A. Advantages, limitations, and future suggestions in studying graphene-based desalination membranes. *RSC Adv.* **2021**, 11, 7981-8002.
31. Bekru, A.G.; Tufa, L.T.; Zelekew, O.A.; Goddati, M.; Lee, J.; Sabir, F.K. Green synthesis of a CuO–ZnO nanocomposite for efficient photodegradation of methylene blue and reduction of 4-nitrophenol. *ACS Omega* **2022**, 7, 30908-30919.
32. Alharthi, F.A.; Alghamdi, A.A.; Al-Zaqri, N. Alanazi, H.S.; Alsyahi, A.A.; Marghany, A.E.; Ahmad, N. Facile one-pot green synthesis of Ag–ZnO nanocomposites using potato peeland their Ag concentration dependent photocatalytic properties. *Sci. Rep.* **2020**, 10, 20229.
33. Etefa, H.F., Nemera, D.J.; Dejene, F.B. Green synthesis of nickel oxide NPs incorporating carbon dots for antimicrobial activities. *ACS Omega* **2023**, 8, 38418-38425.
34. Nemera, D.J.; Etefa, H.F.; Kumar, V.; Dejene, F.B. Hybridization of nickel oxide nanoparticles with carbon dots and its application for antibacterial activities. *Luminescence* **2022**, 37, 965-970.
35. Talipova, A.B.; Buranych, V.V.; Savitskaya, I.S.; Bondar, O.V.; Turlybekuly, A.; Pogrebnjak, A.D. Synthesis, properties, and applications of nanocomposite materials based on bacterial cellulose and MXene. *Polymers* **2023**, 15, 4067.
36. Mousumi, S. *Nanocomposite Materials, in Nanotechnology and the Environment*, 2nd ed., IntechOpen: Rijeka; **2020**; p. Ch. 6.
37. Boukhoubza, I.; Khenfouch, M.; Achehboune, M.; Leontie , L.; Galca, A.C.; Enculescu, M.; Carlescu, A.; Guerboub, M.; Mothudi, M.B.; Jorio, A.; Zorkani, I. Graphene oxide concentration effect on the optoelectronic properties of ZnO/GO nanocomposites. *Nanomaterials* **2020**, 10, 1532.
38. Zaabaa, N.I.; Fooa, K.L.; Hashima, U.; Tanb, S.J.; Liua , W.W.; Voon, C.H. Synthesis of graphene oxide using modified hummers method: Solvent influence. *Procedia Eng.* **2017**, 184, 469-477.
39. Bokov, D.; Jalil, A.T.; Chupradit, S.; Suksatan, W.; Ansari, M.J.; Shewael, I.H.; Valiev, G.H.; Kianfar, E. Nanomaterial by sol-gel method: Synthesis and application. *Adv. Mater. Sci. Eng.* **2021**, 2021, 5102014.
40. Mendes, C.R.; Dilarri1, G.; Forsan, C.F.; Ruy Sapata, V.M.; Matos Lopes, P.R.; Moraes, P. B.; Montagnolli, R.N., Ferreira, H.; Bidoia, E.D. Antibacterial action and target mechanisms of zinc oxide nanoparticles against bacterial pathogens. *Sci. Rep.* **2022**, 12, 2658.
41. Naseer, Q.A.; Xue, X.; Wang, X.; Dang, S.; Din, S.U.; Kalsoom, Jamil, J. Synthesis of silver nanoparticles using *Lactobacillus bulgaricus* and assessment of their antibacterial potential. *Braz. J. Biol.* **2021**, 82, e232434.
42. Arefi, M.; Rezaei-Zarchi, S. Synthesis of zinc oxide nanoparticles and their effect on the compressive strength and setting time of self-compacted concrete paste as cementitious composites. *Int. J. Mol. Sci.* **2012**, 13, 4340-4350.
43. Siburian, R.; Sihotang, H.; Lumban Raja, S.; Supeno, M.; Simanjuntak, C. New route to synthesize of graphene nano sheets. *Orient. J. Chem.* **2018**, 34, 182-187.

44. Mtavangu, S.G.; Machunda, R.L.; Bruggen, B.V.; Njau, K.N. In situ facile green synthesis of Ag–ZnO nanocomposites using *Tetradenia riperia* leaf extract and its antimicrobial efficacy on water disinfection. *Sci. Rep.* **2022**, 12, 15359.
45. Farah, A.; Tefo, T.F.; Dikio, E. Electrochemical detection of hydrogen peroxide based on graphene oxide/prussian blue modified glassy carbon electrode. *Int. J. Electrochem. Sci.* **2012**, 7, 5069-5083.
46. Sudesh; Kumar, N.; Das, S.; Bernhard, C.; Varma, G.D. Effect of graphene oxide doping on superconducting properties of bulk MgB_2. *Supercond. Sci. Technol.* **2013**, 26, 095008.
47. Çiplak, Z., Yildiz, N.K. Çalimli, A. Investigation of graphene/Ag nanocomposites synthesis parameters for two different synthesis methods. *Fuller. Nanotubes Carbon* **2014**, 23, 361-370.
48. Azeez1, F.; Al-Hetlani, E.; Arafa, M.; Abdelmonem, Y.; Nazeer, A.A.; Amin, M.O.; Madkour, M. The effect of surface charge on photocatalytic degradation of methylene blue dye using chargeable titania nanoparticles. *Sci Rep.* **2018**, 8, 7104.
49. Bedlovičová, Z.; Strapáč, I.; Baláž, M.; Salayová A. A brief overview on antioxidant activity determination of silver nanoparticles. *Molecules* **2020**, 25, 3191.
50. Rashad, M.; Mahfoz Kotb, H.; Helali, S.; Ahmad, M.M.; Albalawi, A.E.; Alatawi, N.S.; Al-Faqiri, B.; Alsharari, A.M.; Abd-Elnaiem, A.M. Structural analysis and photocatalytic degradation towards methylene blue using $(Nb_{0.5}Si_{0.5})_xTi_{1-x}O_2$ nanocomposites. *Ceram. Int.* **2024**, 50, 512-525.